Computational Validation of a Two-dimensional Semi-empirical Model for Inductive Coupling in a Conical Pulsed Inductive Plasma Thruster*

JANNAF-2011-2197

Presented at the Joint Army-Navy-NASA-Air Force (JANNAF) 8th MSS / 6th LPS / 5th SPS Meeting
Huntsville, Alabama, December 5-9, 2011

Ashley K. Hallock†
Yetispace Inc.
Huntsville, AL 35812

Kurt A. Polzin‡
NASA-Marshall Space Flight Center
Huntsville, AL 35812

A two-dimensional semi-empirical model of pulsed inductive thrust efficiency is developed to predict the effect of such a geometry on thrust efficiency. The model includes electromagnetic and gas-dynamic forces but excludes energy conversion from radial motion to axial motion, with the intention of characterizing thrust efficiency loss mechanisms that result from a conical versus a flat inductive coil geometry. The range of conical pulsed inductive thruster geometries to which this model can be applied is explored with the use of finite element analysis. A semi-empirical relation for inductance as a function of current sheet radial and axial position is the limiting feature of the model, restricting the applicability as a function of half cone angle to a range from ten degrees to about 60 degrees. The model is nondimensionalized, yielding a set of dimensionless performance scaling parameters. Results of the model indicate that radial current sheet motion changes the axial dynamic impedance parameter at which thrust efficiency is maximized. This shift indicates that when radial current sheet motion is permitted in the model longer characteristic circuit timescales are more efficient, which can be attributed to a lower current sheet axial velocity as the plasma more rapidly decouples from the coil through radial motion. Thrust efficiency is shown to increase monotonically for decreasing values of the radial dynamic impedance parameter. This trend indicates that to maximize the radial decoupling timescale should be long compared to the characteristic circuit timescale.

Nomenclature

C	capacitance (F)	R_p, R_e	plasma, external resistance (Ω)
E	energy (J)	r_{coil}, $\overline{r_{coil}}$	coil minor, average radius (m)
F	force (N)	T_1	upstream temperature (K)
I_1, I_2	coil, plasma current (A)	u	shock velocity (m/s)
k	Boltzmann's constant (J K^{-1})	V, V_0	voltage, initial capacitor voltage (V)
L_0, L_C, L_{tot}	initial, coil, total inductance (H)	v_r, v_z	radial, axial slug velocity (m s^{-1})
L^*	nondimensional inductance	z	axial location (m)
l_{coil}	coil length (m)	z_0	axial decoupling distance (m)
M	mutual inductance (H)	α	axial dynamic impedance parameter

*Statement A: Approved for public release. Distribution is unlimited.

†Senior Engineer, Electric Propulsion Department, Ashley.K.Hallock@nasa.gov.

‡Propulsion Research Engineer, Propulsion Research and Technology Applications Branch,Propulsion Systems Department, Kurt.A.Polzin@nasa.gov

$\mathcal{M}$	Mach number	γ	specific heat ratio
m_i, m_{bit}	ion mass, slug mass (kg)	ϕ	radial dynamic impedance parameter
P_1, P_2	upstream, downstream pressure (Pa)	ψ_1, ψ_2	critical resistance ratios
$r, \bar{r}$	radial, average radial location (m)	Ξ	gas-dynamic pressure parameter

I. Introduction

It is desirable to extend the lifetime and increase the reliability of an in-space propulsion system as much as possible since maintenance or replacement of that system becomes particularly challenging once it has been placed into orbit. Reducing the size and mass of the propulsion system, including the propellant required to complete a mission, can permit an increase in the amount of payload as a percentage of total vehicle mass. The high values of specific impulse associated with electric propulsion (EP) reduces the amount of propellant needed for a given mission relative to other conventional propulsion systems.

Pulsed inductive plasma thrusters[1–3] are spacecraft propulsion devices in which electrical energy is capacitively stored and then discharged through an inductive coil. The thruster is electrodeless, with a time-varying current in the coil interacting with a plasma covering the face of the coil to induce a plasma current. Propellant is accelerated and expelled at a high exhaust velocity ($\mathcal{O}(10 - 100$ km/s)) by the Lorentz body force arising from the interaction of the magnetic field and the induced plasma current.

Thrusters of this type possess many demonstrated and potential benefits that make them worthy of continued investigation. The electrodeless nature of these thrusters eliminates the lifetime and contamination issues associated with electrode erosion in conventional electric thrusters. Also, a wider variety of propellants are available for use when compatibility with metallic electrodes is no longer an issue. Pulsed inductive accelerators have been successfully operated using propellants like ammonia, hydrazine, and CO_2, and there is no fundamental reason why they would not operate on other propellants like H_2O. It is well-known that pulsed accelerators can maintain constant specific impulse, $I_{\rm sp}$, and thrust efficiency, η_t, over a wide range of input power levels by adjusting the pulse rate to maintain a constant discharge energy per unit pulse. It has also been demonstrated that a pulsed inductive thruster operating in or near the regime of optimum dynamic impedance matching can operate at a relatively constant thrust efficiency over a wide $I_{\rm sp}$ range. Thrusters in this class have operated at high energy per pulse, and by increasing the pulse rate they offer the potential to process very high levels of power using a single thruster.

It has been found [1,2,4] that propellant utilization inefficiency can be a disadvantage for pulsed inductive thrusters with a flat inductive coil geometry. One proposed solution is the use of a nozzle downstream of the accelerating coil that injects propellant upstream onto the face of the inductive coil. This solution, however, presents the additional disadvantage of placing a physical body in the exhaust path of the propellant, adversely altering the propellant trajectory as the exhaust impacts and, over time, erodes the propellant injection structure.

A possible alternative solution to this problem is to alter the inductive coil geometry to better confine the neutral propellant within the region of interest where the processes of current sheet formation and acceleration occur. One alternative to a flat coil is a conic section or conical frustum. A flat, disc-shaped inductive coil can be considered as a conical inductive coil with a half cone angle of 90°. As the half cone angle is decreased the fraction of axial electromagnetic force on the plasma current sheet decreases as a radial electromagnetic (pinching) force appears and increases. The ability to predict the effect of coil geometry on propellant utilization efficiency and plasma current sheet motion would permit a trade-off study between cone angle and efficiency and aid in the physical understanding and design of this type of thruster.

A model [5] relating two-dimensional plasma current sheet motion and inductive coil geometry has been developed based upon a two-dimensional semi-empirical inductance relation incorporated into a well-known acceleration model [2]. The semi-empirical model yielding inductance as a function of plasma position has been compared to experimental data obtained for a limited range of coil geometries and simulations spanning a broader expanse of the parameter space. In this paper we present the semi-empirical model of inductance as a function of coil angle and current sheet position and show finite element results that support the model's validity. The entire two-dimensional acceleration model is then nondimensionalized and the relevant scaling parameters are discussed in terms of their effect on thrust efficiency.

II. Two-Dimensional Inductive Accelerator Model

Pulsed inductive thrusters are commonly modeled as a circuit [2], shown in Fig. II, where I_1 is the current flowing in the driving circuit, I_2 is the current flowing in the plasma current sheet, C is the capacitance of the capacitor, M is the time-varying mutual inductance between the driving coil and the current sheet, L_0 is the initial (parasitic) inductance, L_C is the accessible coil inductance, R_p is the resistance of the plasma, and R_e is the resistance in the driving circuit.

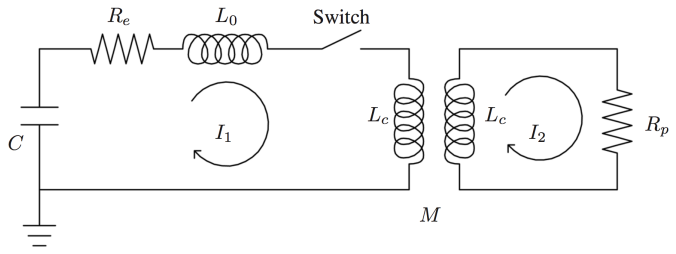

Figure 1. Lumped element circuit model of a pulsed inductive thruster inductively coupled to a plasma (taken from Ref. [2]).

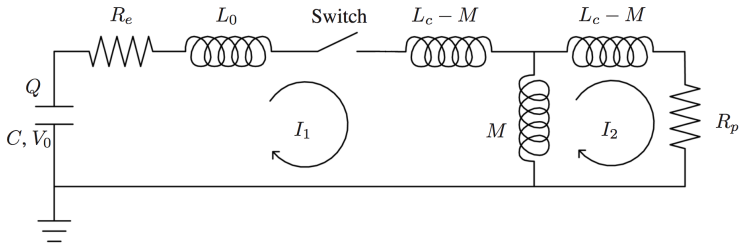

Figure 2. Equivalent circuit of a pulsed inductive thruster inductively coupled to a plasma used to derive a set of governing equations to model thruster performance.

An equivalent circuit, shown in Fig. 2, can be drawn and a set of equations can be written to model thruster performance in terms of the electrical parameters. For this circuit, where V is the voltage on the capacitor as a function of time (initially at V_0), the following equations follow from the application of Kirchoff's law:

$$\frac{dI_1}{dt} = \frac{L_C V - L_C R_e I_1 - M R_p I_2 + (L_C I_2 + M I_1)\frac{dM}{dt}}{L_C\left(L_0 + L_C\right) - M^2} \tag{1}$$

$$\frac{dI_2}{dt} = \frac{M\frac{dI_1}{dt} + I_1\frac{dM}{dt} - R_p I_2}{L_C} \tag{2}$$

$$\frac{dV}{dt} = -\frac{I_1}{C} \tag{3}$$

Neglecting the resistive elemenets and adding the series and parallel lumped inductive elements shown in Fig. 2 gives the total inductance,

$$L_{tot} = L_0 + L_C - \frac{M^2}{L_C}. \tag{4}$$

It can be seen from this equation that the total inductance changes as a function of time due to the mutual inductance term, which varies due to the movement of the current sheet. An expression for the mutual inductance as a function of current sheet axial and radial position has been empirically determined as:

$$L_{tot}(\bar{r}, z) = L_0 + L_C\left(1 - \exp\left(-z/z_0\right)\left(\frac{\bar{r}}{\overline{r_{coil}}}\right)^N\right) \tag{5}$$

where $\bar{r}$ is the average radial position of the current sheet, r_{coil} is the average radial position of the coil, z is the axial displacement of the current sheet, N is a fit parameter found to be close to 2 for all cases studied here, and z_0 is the axial decoupling distance. This expression is set equal to the previous expression for total inductance (Eq. 4) and solved for the mutual inductance as a function of the axial and radial separation distance between the driving coil and the current sheet:

$$M = L_C \exp\left(\frac{-z}{2z_0}\right)\left(\frac{\bar{r}}{\overline{r_{coil}}}\right)^{N/2}, \tag{6}$$

of which the time derivative is,

$$\frac{dM}{dt} = \frac{L_C}{\overline{r_{coil}}^N}\frac{N}{2}\bar{r}^{\frac{N}{2}-1}\frac{dr}{dt}\exp(-z/z_0) - \frac{L_C}{2z_0}\exp\left(-z/2z_0\right)\frac{dz}{dt}\left(\frac{\bar{r}}{\overline{r_{coil}}}\right)^{N/2}, \tag{7}$$

The equation of motion for the current sheet can be written using Newton's second law with the thrust-producing force arising from the magnetic pressure between the driving coil and the current sheet. This force in the arbitrary i^{th}-direction is given as:

$$F_i = \frac{I^2}{2}\frac{\partial L}{\partial x_i}. \tag{8}$$

This force is opposed in the radial direction by a gas-dynamic pressure force P_2 that increases as the current sheet moves toward the thrust axis and is calculated assuming the current sheet acts as a normal shock wave:

$$\frac{P_2}{P_1} = 1 + \frac{2\gamma}{\gamma+1}\left[\mathcal{M}^2 - 1\right] \tag{9}$$

where P_2 is the pressure of the gas downstream of the shock, P_1 is the pressure upstream of the shock, γ is the ratio of specific heats (taken here to be 5/3), and $\mathcal{M}$ is the local Mach number upstream of the shock:

$$\mathcal{M} = u/\sqrt{\frac{\gamma k T_1}{m_i}} \tag{10}$$

where u is the shock velocity in the given direction, k is Boltzmann's constant, T_1 is the temperature of the gas upstream of the shock, and m_i is the mass of an ion.

Using the functional dependence of inductance on both axial and radial position, scalar momentum equations can be written for both axial and radial motion:

$$\frac{dv_z}{dt} = \left[\frac{L_C I_1^2}{2z_0}\exp\left(-\frac{z}{z_0}\right)\left(\frac{\bar{r}}{\overline{r_{coil}}}\right)^N\right]/m_{bit}, \tag{11}$$

$$\frac{dv_r}{dt} = \left[P_2 2\pi\bar{r}l_{coil} - \frac{L_C I_1^2 N}{2\overline{r_{coil}}^N}\exp\left(-\frac{z}{z_0}\right)(\bar{r})^{N-1}\right]/m_{bit}. \tag{12}$$

where m_{bit} is the total propellant mass in the current sheet, v_z is the axial current sheet velocity, and v_r is radial velocity. The axial z and radial r position are related to the axial and radial velocities as:

$$\frac{dz}{dt} = v_z \tag{13}$$

$$\frac{dr}{dt} = v_r. \tag{14}$$

The time-evolution of the pressure P_2 is given by the time-derivative of Eq. 9,

$$\frac{dP_2}{dt} = \frac{P_1 2\gamma}{\gamma+1}\frac{m_i}{\gamma k T_1}2v_r\frac{dv_r}{dt}, \tag{15}$$

bringing the total number of first-order coupled ODEs in the system to nine.

Of the nine equations (Eqs. 1, 2, 3, 7, 11, 12, 13, 14, and 15), six rely on the semi-empirical relation for coil inductance as a function of current sheet location. It should be noted that no attempt is made here to model energy conversion from radial current sheet motion to axial momentum. In addition, this study focuses only on thrust efficiency, making no attempt to model factors such as propellant utilization efficiency that could be a function of coil geometry and would impact the total thruster efficiency.

III. Finite Element Analysis

The inductive coupling between coils and current sheets of various geometries were simulated using finite element analysis to explore the geometric range of validity of Eq. 5. First, the coil inductance L_C and decoupling length z_0 were calculated by curve fitting Eq. 5 to the simulated inductance as a function of axial current sheet position with a constant current sheet radial position roughly equal to ($\overline{r_{coil}}$). Then, the inductance was calculated for various current sheet radial and axial locations, the results of which are shown in Figs. 4, 5, and 6 along with inductance calculations using Eq. 5 where the simulation data are plotted as markers and Eq. 5 is plotted as a red line.

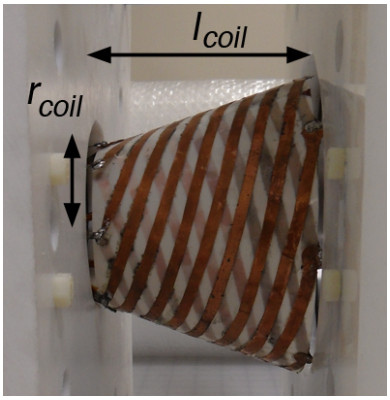

Figure 3. Diagram of the inductive coil geometry.

The coil geometry is shown and labeled in Fig. 3. The geometry is designated in the lower left hand corner of Figs. 4 - 6 where the number is the half cone angle and a suffix of "S", "M" or "L" refers respectively to a short, 5 cm, medium 6-8 cm, or a long, 10 cm coil length l_{coil}. All coils had a minor radius r_{coil} of 4 cm, and the only coil with $l_{coil} = 0$ had a half cone angle of 90°. Agreement between the finite element results and Eq. 5 is good for half cone angles between 20°-55°, as shown in Fig. 5, but begins to breakdown outside this range, as shown in Figs. 4 and 6.

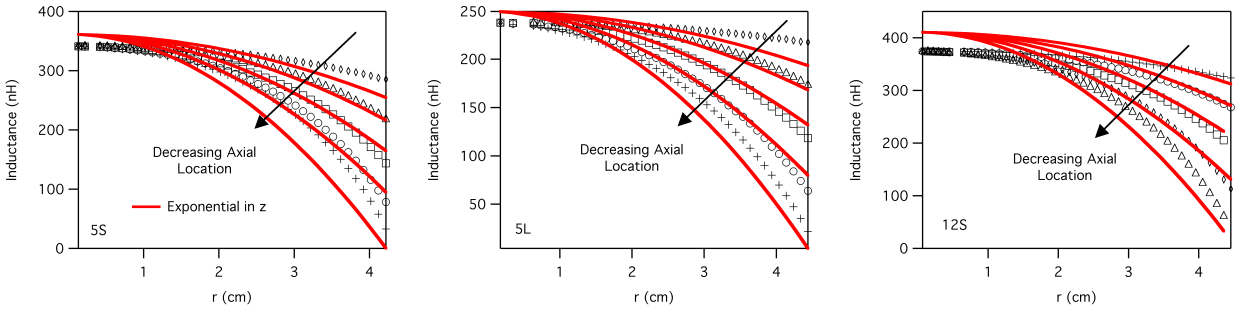

Figure 4. Finite element results (represented by markers) and the semi-empirical model (represented by a red line) for the inductance as a function of average current sheet radial position. Coil geometry is designated in the lower-left corner of the plot.

For coils with a half cone angle below 12°, it is not the radial part of the model that begins to fail but rather the axial part. The inductance as a function of axial current sheet location is fit more accurately by an error function than an exponential, as shown in Fig. 7.

Plots of the inductance as calculated using the error function in place of the exponential in Eq. 5 are compared in Fig. 8 to inductance calculations using Eq. 5. Below half cone angles of 12°, the discrepancies in the results of two semi-empirical equations for inductance increase with decreasing half cone angle, with the exponential function providing a poorer fit to the finite element inductance results.

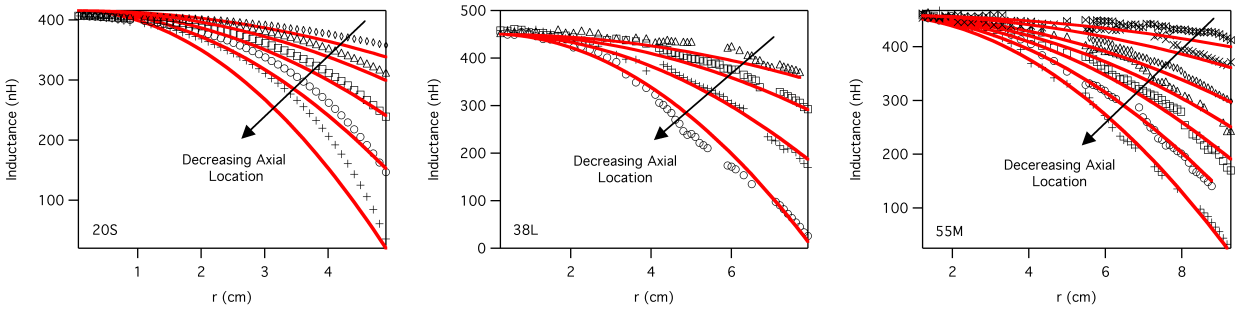

Figure 5. Finite element results (represented by markers) and Eq. 5 (represented by a red line) for the inductance as a function of average current sheet radial position. Coil geometry is designated in the lower-left corner of the plot.

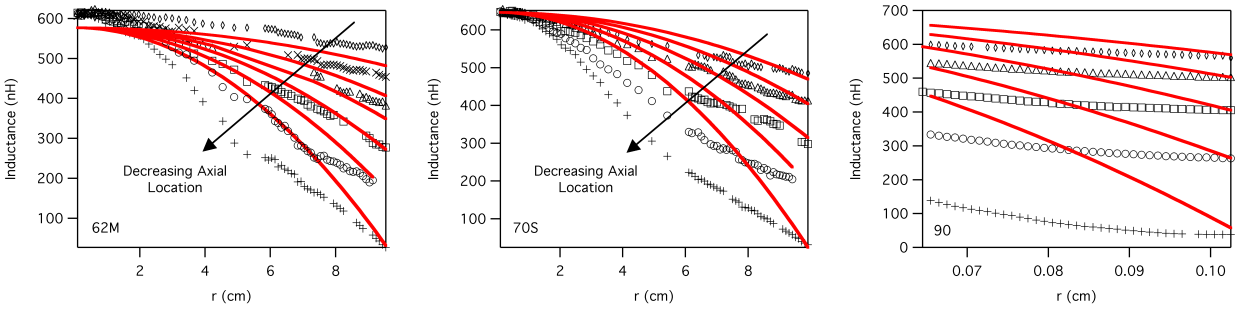

Figure 6. Finite element results (represented by markers) and Eq. 5 (represented by a red line) for the inductance as a function of average current sheet radial position. Coil geometry is designated in the lower-left corner of the plot.

IV. Nondimensional Solution Approach

The following substitutions can be made to nondimensionalize the equation set from Section II following Refs. [6, 7]:

$$
\begin{aligned}
I_1^* &= \frac{1}{V_0}\sqrt{\frac{L_C}{C}}I_1 & I_2^* &= \frac{1}{V_0}\sqrt{\frac{L_C}{C}}I_2 \\
V^* &= \frac{V}{V_0} & M^* &= \frac{M}{L_C} \\
v_z^* &= \frac{\sqrt{L_0 C}}{z_0}v_z & z^* &= \frac{z}{z_0} \\
v_r^* &= \frac{\sqrt{L_0 C}}{r_{coil}}v_r & r^* &= \frac{r}{r_{coil}} \\
t^* &= \frac{t}{\sqrt{L_0 C}} & P^* &= \frac{P}{P_1}
\end{aligned}
\tag{16}
$$

Applying these substitutions to Eqns. 1, 2, 3, 7, 11, 12, 13, 14, and 15 yields the following nondimensional

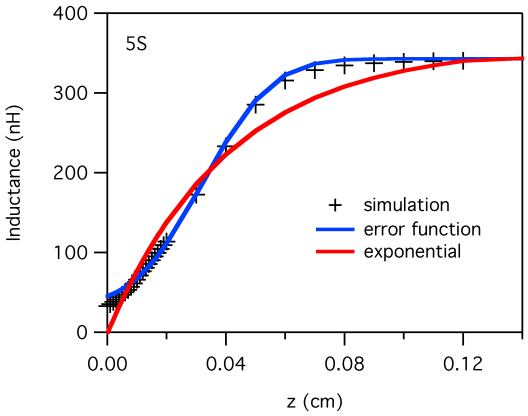

Figure 7. Comparison between the functional form of fits for the inductance as a function of current sheet axial location. Exponential fits are shown in red and error function fits are shown in blue.

equation set:

$$
\begin{aligned}
\frac{dI_1^*}{dt^*} &= \left[L^*V^* + (M^*I_1^* + I_2^*)\frac{dM^*}{dt^*} - \psi_2 L^* I_2^* M^* - \psi_1 L^* I_1^*\right] / \left(L^* + 1 - {M^*}^2\right) \\
\frac{dI_2^*}{dt^*} &= M^*\frac{dI_1^*}{dt^*} + I_1^*\frac{dM^*}{dt^*} - I_2^* L^* \psi_2 \\
\frac{dV^*}{dt^*} &= -I_1^* \\
\frac{dM^*}{dt^*} &= \frac{N}{2}{r^*}^{\frac{N}{2}-1} v_r^* \exp(-\frac{z^*}{2}) - \frac{1}{2}{r^*}^{\frac{N}{2}} v_z^* \exp(-\frac{z^*}{2}) \\
\frac{dv_r^*}{dt^*} &= \lambda P^* r^* - \phi {I_1^*}^2 {r^*}^{N-1} \exp(-z^*) \\
\frac{dr^*}{dt^*} &= v_r^* \\
\frac{dv_z^*}{dt^*} &= \alpha {I_1^*}^2 {r^*}^N \exp(-z^*) \\
\frac{dP^*}{dt^*} &= \Xi v_r^* \frac{dv_r^*}{dt^*}
\end{aligned}
\tag{17}
$$

The terms α, ψ_1, ψ_2, ϕ, λ, and Ξ are the relevant nondimensional scaling parameters of the system, and are defined as:

$$
\begin{aligned}
\alpha &= \frac{V_0^2 C^2 L_C}{2 m_{bit} z_0^2} & \psi_1 &= R_e\sqrt{\frac{C}{L_0}} \\
\psi_2 &= R_p\sqrt{\frac{C}{L_0}} & \phi &= \frac{V_0^2 C^2 L_C}{2 m_{bit} \overline{r_{coil}}^2} \\
\lambda &= \frac{L_0 C P_1 2\pi l_{coil}}{2 m_{bit}} & \Xi &= \frac{4\gamma}{\gamma+1}\frac{m_i}{\gamma k T_1}\frac{1}{r_{coil}^2 L_0 C} \\
L^* &= \frac{L_0}{L_C}
\end{aligned}
\tag{18}
$$

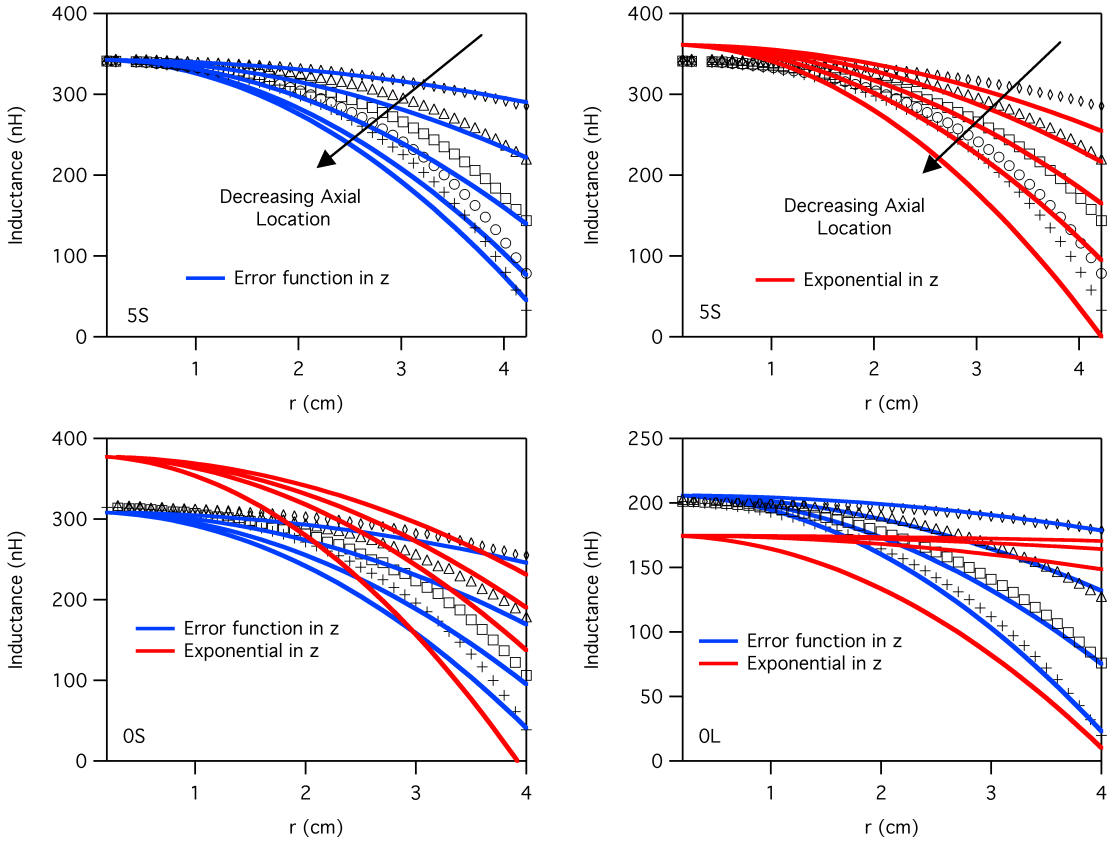

Figure 8. Comparison of the accuracy of two functional fits for the inductance as a function of current sheet axial and radial locations. Exponential fits are shown in red and error function fits are shown in blue.

V. Model Results and Discussion

The parameters ψ_1 and ψ_2 are critical resistance ratios, affecting the damping of the current in the driving circuit, and L^* is a ratio of the initial (or inaccessible) inductance to the accessible inductance, representing a measure of the fraction of input electromagnetic energy that can be transferred to acceleration of the current sheet. The physical interpretations of these three parameters remains unchanged as compared to those of previous studies of pulsed inductive plasma thrusters with flat inductive coil geometries, and more information on them can be found in Refs. [6, 7].

λ appears as a new parameter in this model, and affects the force opposing radial current sheet motion caused by the gas-dynamic pressure acting in the positive radial direction along the inner surface of the current sheet. Ξ is another new parameter, and is a measure of the growth rate of this gas-dynamic pressure as the current sheet shock front undergoes radial acceleration. For the following calculations, $\psi_1 = 0.05$, $\psi_2 = 0.01$, $L^* = 0.18$, $\lambda = 7.0 \cdot 10^{-7}$, and $\Xi = 2.3 \cdot 10^4$.

The parameter α can be expanded into a product of physically meaningful ratios [6]:

$$\alpha = \frac{C^2 V_0^2 L_C}{2 m_{bit} z_0^2} = \frac{1}{8\pi^2} \frac{C V_0^2/2}{m_{bit} v_z^2/2} L^* \left(\frac{2\pi\sqrt{L_0 C}}{L_0/\dot{L}_z} \right)^2$$

where $\dot{L}_z = v_z L'_z$ and $L'_z = L_C/z_0$. The second ratio on the right hand side represents the inverse of thrust efficiency, the third term represents a ratio of the initial inductance in the pulse circuit to the coil inductance, which places a limit on the achievable thrust efficiency through the Lovberg criterion [8]. The fourth ratio represents a balance between the characteristic ringing time of the driving circuit and the characteristic time over which the current sheet remains electromagnetically coupled to the driving circuit. In other words, the parameter α is a measure of the dynamic impedance match between the driving circuit and the axially-moving current sheet. It has been shown that there exists an optimum α for which η_t is maximized, corresponding

to a pulsed inductive plasma thruster that is dynamically impedance matched [9].

Thrust efficiency can be related to α by the following relation:

$$\eta_t = \frac{{v_z^*}^2}{2L^*\alpha}.$$

For systems constrained to axial motion (zero radial motion) the optimum value of α for maximum η_t is between one and three [10]. When the current sheet is axially accelerated at a fixed radial position that is less than $\overline{r_{coil}}$ ($v_r^* = 0$ and $r^* = A \,\forall\, t^*$ where $0 < A \leq 1$), the absolute value of η_t decreases and the maximum η_t occurs at a higher value of α, as shown in Fig. 9. As shown in the figure, the maximum achievable η_t is lower as the sheet is displaced closer to the centerline.

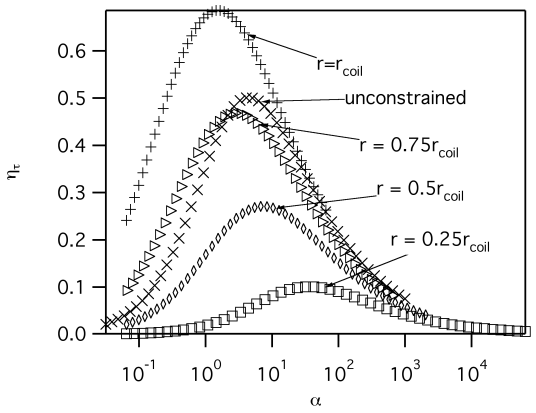

Figure 9. Calculated thrust efficiency as a function of α for different radial current sheet displacements.

A possible explanation for the shift in optimum values of α is that as the current sheet displaces radially, it slows the axial acceleration of the current sheet. This causes a longer current sheet residence time in practice, but that information is not contained in α. Consequently, a longer characteristic circuit time, which will increase the value of α, represents a better dynamic impedance match.

The parameter ϕ can be similarly expanded:

$$\phi = \frac{C^2V_0^2L_C}{2m_{bit}r_{coil}^2} = \frac{1}{8\pi^2}\frac{CV_0^2/2}{m_{bit}v_r^2/2}L^*\left(\frac{2\pi\sqrt{L_0C}}{L_0/\dot{L}_r}\right)^2$$

where $\dot{L}_r = v_rL_r'$ and $L_r' = L_C/\overline{r_{coil}}$. The second term does not represent thrust efficiency, as in the expansion for α, but rather the inverse of the fraction of total energy that is converted into radial kinetic energy. The fourth term represents a balance between the characteristic circuit time and the characteristic time over which radial (not axial) current sheet motion causes electromagnetic decoupling from the driving circuit.

While an efficient coupling of energy into the axial direction is beneficial to thrust efficiency, efficient coupling of energy into the radial direction has a generally detrimental effect on thrust efficiency unless some means exists to efficiently convert the radial motion to axial thrust. If the radial dynamic impedance mismatch were caused by a small timescale of radial current sheet decoupling compared to the timescale of the driving circuit, the current sheet would decouple before the driving circuit had an opportunity to transfer initial circuit energy into axial current sheet motion. Therefore, thrust efficiency should be optimized for a condition where the timescale over which the current sheet radially decouples from the driving circuit is long compared to the characteristic time of the driving circuit, leading to faster decoupling due to axial motion instead of radial motion. This would indicate an increase in η_t for decreasing values of ϕ, a trend that can be seen in the plot of η_t versus ϕ for $\alpha = 0.6$, shown in Fig. 10.

A contour plot of the combined effects of the two dynamic impedance parameters is shown in Fig. 11. As ϕ increases, the thrust efficiency decreases for all values of α due to faster current sheet decoupling from the driving circuit, resulting in lower achievable axial propellant velocity. The efficiency is optimized at higher values of α as ϕ is increased, in agreement with Fig. 9.

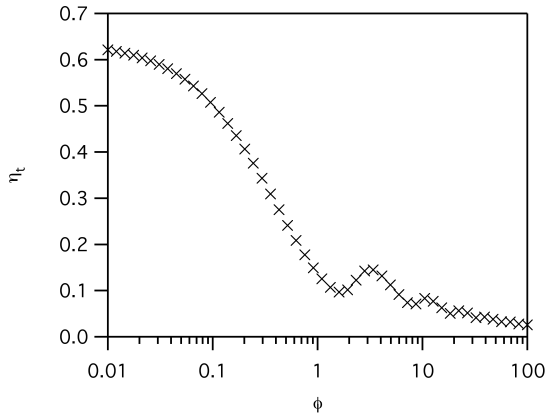

Figure 10. Model results of thrust efficiency as a function of ϕ for the unconstrained case with $\alpha = 0.6$.

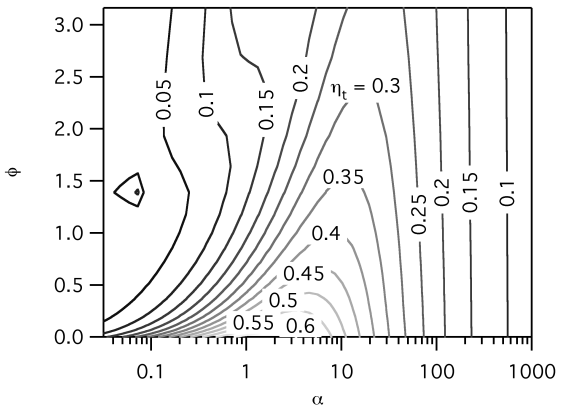

Figure 11. Contour plot of thrust efficiency as a function of α and ϕ.

VI. Conclusions

In this paper we presented a two-dimensional semi-empirical acceleration model for pulsed inductive plasma thrusters. The semi-empirical aspects of the model were validated through a combination of measurements and finite element modeling of the inductance of coil geometries with a minor radius of 4 cm where the half cone angles were between 20°-55° and the coil lengths ranged from 5-10 cm. The model was nondimensionalized and two of the nondimensional scaling parameters, namely the axial and radial dynamic impedance parameters, were discussed. Contour plots of thrust efficiency as a function of these two parameters were presented. Trends in these plots indicate that as ϕ is increased, thrust efficiency is optimized at greater values of α. This is explained by a slower axial current sheet acceleration and consequently a longer axial acceleration timescale due to radial current sheet displacement, which results in a better dynamic impedance match occurring for a longer characteristic circuit time. In the present model with no mechanism to convert radial kinetic energy to directed axial thrust, efficiency is maximized for smaller values of the radial dynamic impedance parameter, indicating that higher axial current sheet velocity is achieved when the current sheet decouples slowly in the radial direction compared to the characteristic time of the driving circuit.

Acknowledgments

The authors appreciate the help and support of Mr. Adam Kimberlin, Dr. Adam Martin, Dr. Noah Rhys, Mr. J. Boise Pearson, and Mr. Jim Martin. This work was supported in part by NASA's Advanced

In-Space Propulsion program managed by Dr. Michael LaPointe and the Office of the Chief Technologist In-Space Propulsion Program managed by Mr. Timothy Smith.

References

[1]Polzin, K. A. Comprehensive review of planar pulsed inductive plasma thruster research and technology. *Journal of Propulsion and Power*, 27(3):513–531, May-June 2011.

[2]Lovberg, R. H. and Dailey, C. L. A PIT primer. Technical Report 005, RLD Associates, Encino, CA, 1994.

[3]Dailey, C. L. and Lovberg, R. H. The PIT MkV Pulsed Inductive Thruster. Technical Report 191155, Lewis Research Center, Redondo Beach, CA, July 1993.

[4]Polzin, K. A. Rose, M. F. and Miller, R. Operational Characteristics of a Low-Energy FARAD Thruster. Number AIAA 2008-5011, July 2008.

[5]Hallock, A. K. Polzin, K. A. and Emsellem, G. D. Two-dimensional Analysis of Conical Pulsed Inductive Plasma Thruster Performance. Number IEPC-2011-145, September 2011.

[6]R. G. Jahn. *Physics of Electric Propulsion*. McGraw-Hill Book Company, 1968.

[7]Polzin, K. A. *Faraday Accelerator with Radio-frequency Assisted Discharge (FARAD)*. Ph.D. dissertation, Princeton University, Department of Mechanical and Aerospace Engineering, 2006.

[8]Gooding, T. Lovberg, R. H., Hayworth, B. R. The Use of a Coaxial Gun for Plasma Propulsion. Technical Report AE62-0678, G. D. Convair, 1962.

[9]Polzin, K. A. Scaling and System Considerations in Pulsed Inductive Plasma Thrusters. *IEEE Transactions on Plasma Science*, 36(5):2189–2198, October 2008.

[10]K. A. Polzin and E. Y. Choueiri. Performance optimization criteria for pulsed inductive plasma acceleration. *IEEE Transactions on Plasma Science*, 34(3):945–953, 2006.